SOFT ROBOTS

Soft deployable airless wheel for lunar lava tube intact exploration

Seong-Bin Lee[1]†, Namsuk Cho[2,3]†, Geonho Lee[3], Seungju Lee[3], Junseo Kim[1], Gyujin Shim[4], Jong Tai Jang[4], Se Kwon Kim[5], TaeWon Seo[6], Chae Kyung Sim[7,8], Dae-Young Lee[1]*

Lunar pits and lava tubes hold promise for future human habitation, offering natural protection and stable environments. However, exploring these sites entails challenging terrain, including steep slopes along cave funnels and vertical cliffs. Here, we present a soft, deployable airless wheel to address these challenges. By achieving a high deployment ratio, multiple rovers can be stowed efficiently without sacrificing mobility, thereby improving mission reliability and flexibility. The proposed wheel incorporates a reconfigurable reciprocal structure of elastic steel strips arranged in a woven helical pattern, enabling shape transformations while preserving load-bearing capacity. This reciprocal arrangement also allows for safe vertical descents and mitigates damage from accidental falls in caves. By distributing strain throughout the wheel's body, reliance on delicate mechanical components is minimized—a critical advantage under extreme lunar conditions. The wheel can be stowed at a diameter of 230 millimeters and deployed to 500 millimeters. Experimental results show successful traversal of 200-millimeter obstacles, stable mobility on rocky and lunar soil simulant surfaces, and resilience to drop impacts simulating a 100-meter descent under lunar gravity. These findings underscore the wheel's suitability for future pit and cave exploration, even in harsh lunar environments.

INTRODUCTION

The Moon, Earth's closest celestial neighbor, offers a wealth of scientific data for understanding the origins of the universe and abundant natural resources and serves as a pivotal stepping stone for deep space exploration. Among the many intriguing lunar features, lunar pits and caves, formed by collapses of subsurface voids, are considered particularly promising sites for long-term human habitation because they offer natural protection from cosmic radiation, (micro)meteorites, and extreme temperature variations (*1*–*6*). Data from Diviner Lunar Radiometer shows that Mare Tranquillitatis and Mare Ingenii pits are about 100 K warmer than the surrounding surface at night and ~20 K warmer at daily peak, thereby mitigating temperature variations (*7*). Furthermore, volatile stability increases inside pits in permanently shadowed regions, making them ideal for storing and protecting lunar water ice (*8*). Subsequent analyses of surface images across the Moon by Lunar Reconnaissance Orbiter Narrow Angle Camera, using a shadow detection algorithm, revealed over 300 pits. These pits typically have diameters ranging from ~10 to 300 m and depths of about 100 m. They feature a funnel-shaped top and nearly vertical walls transitioning to the bottom, which is not necessarily flat (*5*, *9*).

Several initiatives have proposed missions to investigate these subsurface lava tubes. The European Space Agency developed the Descent And Exploration in Deep Autonomy of Lava Underground Structures probe in collaboration with the University of Würzburg, incorporating three-dimensional (3D) Light Detection And Ranging (LiDAR) and stereo cameras to produce detailed cave maps (*10*, *11*). Researchers at the University of Oviedo proposed deploying a swarm of small robots via a crane, using wireless power transmission to overcome the challenges posed by limited solar illumination (*12*). NASA's Moon Diver mission, with its Axel rover, plans to descend deep pits using rappelling techniques to examine exposed stratigraphy through a suite of scientific instruments (*13*). Canadensys is investigating gravimetric surveying techniques for rover-based scouting and mapping (*14*), and the German Research Center for Artificial Intelligence has proposed a semiautonomous rover that uses a tether system for power and communication (*15*). However, these rappel-centric strategies may introduce risks for multirover missions, such as technical complexity in deployment and safety concerns related to deploying rappelling equipment on a pit funnel.

Although robotic technologies have been continuously developed to enable exploration of extreme environments such as the deep sea (*16*, *17*), ice worlds (*18*), and planetary surfaces (*19*), steep inclines, unstable terrain, and uncharted voids still pose substantial obstacles. Consequently, there is a need for innovative robotic platforms capable of approaching, entering, and conducting interior investigations without relying on additional, complex, heavy equipment. To address a range of mobility challenges, extensive research efforts have focused on advancing the locomotion capabilities of ground-based exploration robots (*20*–*22*). In particular, augmenting conventional circular wheels with reconfigurable or soft structures has emerged as a promising avenue for enhancing adaptability to unpredictable terrains, thereby increasing obstacle-negotiation capabilities and broadening operational parameters across a wide range of terrestrial environments (*23*).

Many shape-change wheel structures developed to date rely on rigid mechanisms, such as origami-inspired folds (*24*) or rotational hinges (*25*). Although these articulated designs enable efficient shape transformation, the exposed joints are often vulnerable to mechanical

[1]Department of Aerospace Engineering, Korea Advanced Institute of Science and Technology (KAIST), Daejeon, 34141, Republic of Korea. [2]Department of Intelligent Robot Engineering, Hanyang University, Seoul, 04763, Republic of Korea. [3]Unmanned Exploration Laboratory, Daejeon, 34126, Republic of Korea. [4]Korea Aerospace Research Institute, Daejeon, 34133, Republic of Korea. [5]Department of Physics, Korea Advanced Institute of Science and Technology (KAIST), Daejeon, 34141, Republic of Korea. [6]School of Mechanical Engineering, Hanyang University, Seoul, 04763, Republic of Korea. [7]Korea Astronomy and Space Science Institute, Daejeon, 34055, Republic of Korea. [8]University of Science and Technology, Daejeon, 34113, Republic of Korea.
*Corresponding author. Email: ae_dylee@kaist.ac.kr
†These authors contributed equally to this work.

shocks, contamination, and environmental hazards such as sharp debris or lunar regolith, making reliable operation in harsh extraterrestrial environments difficult. Soft wheels have been used previously, most notably in the Apollo Lunar Roving Vehicle (*26*), and continue to be studied for space applications (*27*–*31*). These designs aim to enhance traversability in regolith terrain by distributing the vehicle's weight and preventing sinkage. However, achieving enough displacement for large contact areas typically requires oversized wheel diameters, which are unsuitable for compact or lightweight robotic platforms. Soft deformable wheel structures have focused on variable stiffness functionality, allowing adaptability to terrain (*32*, *33*). Yet, such systems often require additional actuators to adjust stiffness, increasing structural complexity. Such complexity can reduce mission reliability, particularly in harsh environments like space, where direct human intervention is not feasible. Soft wheel designs that enable volume change often incorporate localized fabric membranes or textile bellows (*34*). These low-strength textile components can compromise overall durability. Given that the structural integrity of such systems depends on their weakest element, even minor damage may lead to catastrophic failure—an unacceptable risk in planetary exploration scenarios. Therefore, there remains a critical need for compact, robust, impact-resistant soft wheel systems that can provide sufficient traversability without compromising durability, particularly for missions in extreme planetary environments.

In this study, we present a soft, deployable airless wheel with a reconfigurable reciprocal structure, designed for multirover lunar pit exploration. The wheel integrates elastic steel strips in a crossed-helical configuration, enabling continuum-based shape transformation without relying on conventional mechanical joints such as hinges or bearings—an essential advantage in the Moon's extreme environment. This design achieves a high deployment ratio while maintaining robust mobility over rugged terrain near pit entrances and caves (*35*–*38*). The reciprocal arrangement of crossed strips further improves load-bearing capacity and impact resistance, leading to anisotropic behavior: Although the strips coil radially for compact stowage, they resist deformation under vertical loads, providing mutual structural support and preventing collapse during drops or vertical descents into pits. By preserving mobility in these conditions, the wheel reduces reliance on complex access systems, such as rappelling or crane-based systems. Prototype tests demonstrated expansion of the wheel diameter from 230 to 500 mm, successful traversal of 200-mm obstacles and simulated lunar soil terrain, and impact tolerance equivalent to an ~100-m lunar descent, validating its potential for future lunar pit exploration (Movie 1).

RESULTS

Concept of operations for intact exploration of lunar lava tubes

Lunar pits present a unique opportunity to investigate the Moon's near-surface geology and volcanic history. Their steep interior walls expose stratified bedrock, such as lava flows, paleoregolith layers, and impact-related deposits, without the need for heavy equipment like drills (*4*, *6*, *13*, *39*). Some pits may open into subsurface voids or lava tubes, preserving pristine materials from space weathering and potentially harboring volatiles such as water ice (*2*, *4*, *5*, *9*, *40*). To explore these features, compact payloads including stereo imagers, LiDAR, and spectrometers can be used to map 3D pit geometry and analyze mineral composition. Instruments for radiation, temperature, and geophysical sensing can further characterize the internal environment and evaluate the potential of these sites as natural shelters.

These scientific motivations call for a subsurface-access strategy that can navigate complex pit terrains while minimizing mission risk, particularly in hazardous environments where conventional single, primary rover systems may prove vulnerable. Figure 1 illustrates a hypothetical mission scenario for lunar pit exploration, emphasizing the potential operational benefits afforded by the proposed deployable wheel design. In the initial stage, multiple microrovers, referred to as "explorers," would be deployed from a larger base rover, the "carrier." Conventional missions that rely on a single, instrument-laden rover face elevated risks of total mission failure if that rover malfunctions, particularly in hostile environments such as lunar pits. In contrast, deploying multiple smaller rovers would disperse this risk and enhance operational flexibility. However, reducing rover size to accommodate more units typically constrains wheel dimensions, thereby limiting maneuverability over rugged cave terrain. The proposed deployable wheel design would overcome this challenge, enabling the carrier to transport multiple explorers without compromising mobility. To guide the derivation of the wheel's design requirements, we outline a hypothetical mission scenario and corresponding concept of operations for the explorers.

First, once deployed, the explorers would traverse the sloping regions around pit entrances, where maintaining robust traction is crucial to avoid sinkage in loose regolith. Although the explorers remain compact when stowed, the large diameter of the deployable wheels is expected to increase the ground contact area, thereby improving traction on thick dust and uneven slopes. This capability would allow the explorers to navigate challenging pit entrance terrain safely.

Upon reaching the pit rim, the explorers would proceed to the subsurface by descending steep vertical cliffs. Owing to the wheels' elasticity and impact capacity, a direct drop deployment could be feasible, obviating the need for complex rappel systems. This strategy would lower overall risk by keeping the carrier at a safe distance

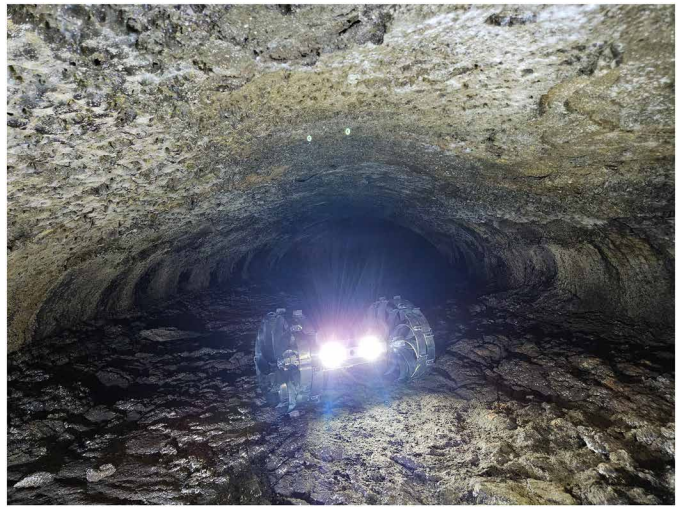

Movie 1. Overview of a soft deployable airless wheel for lunar lava tube exploration. This video provides an overview of the mission sequence for exploring lunar lava tubes and the proposed wheel architecture designed to carry it out. Field demonstrations show the key capabilities required at each mission stage, including pit approach and exploration.

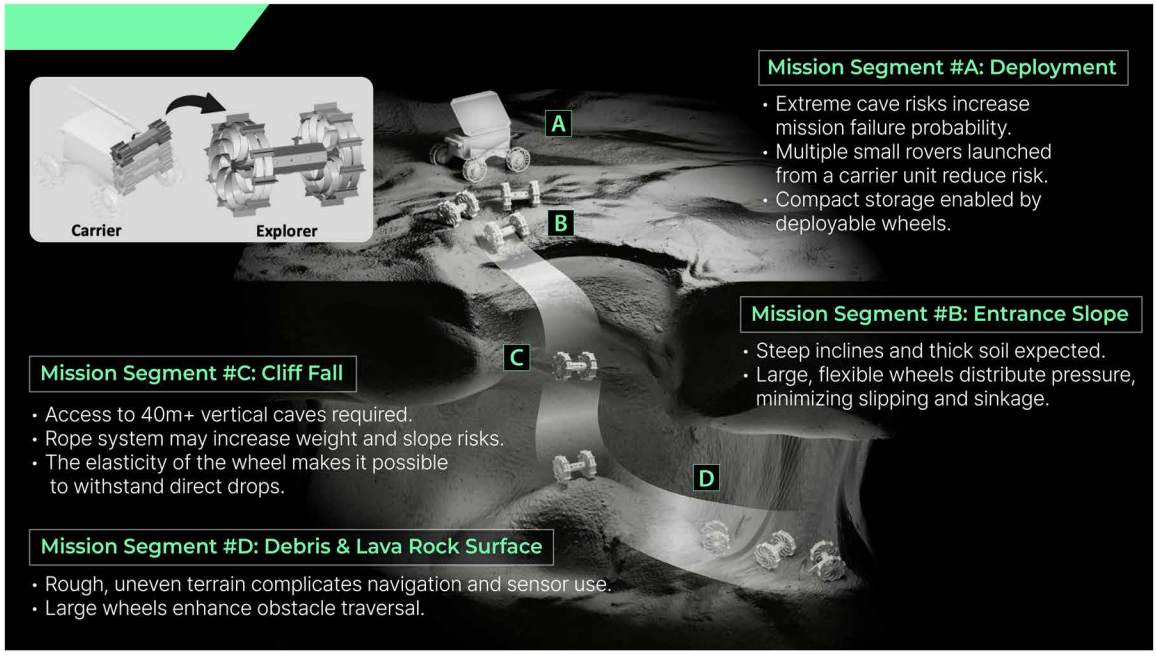

Fig. 1. Lunar pit exploration mission scenario. A mission scenario was proposed for entering and exploring lunar pits, and the four key operational segments necessary for its implementation are described. (**A**) "Deployment" focused on mitigating extreme cave risks by launching multiple compact rovers equipped with deployable wheels from a carrier unit. (**B**) "Entrance Slope" tackled steep inclines and dense soil, leveraging large, flexible wheels that distribute pressure to reduce slippage and sinkage. (**C**) "Cliff Fall" targeted vertical drops exceeding 40 m; in contrast, a rope system may introduce additional mass and cause slope instability, the wheel's elastic properties help it withstand the impact of direct falls. (**D**) "Debris and Lava Rock Surface" ensured robust navigation over rough, uneven terrain, where oversized wheels facilitate the negotiation of obstacles.

from the pit edge while also reducing the mass and operational complexity associated with rappel equipment—an especially valuable advantage when multiple rovers are deployed.

Last, once inside the pit, the explorers would undertake subsurface investigations, where they might encounter sharp undulations and unpredictable rocky steps. The large, highly elastic wheels are expected to excel at surmounting abrupt variations in elevation, ensuring stable and reliable performance despite the harsh subterranean conditions. This robust mobility ultimately underscores the potential of the proposed wheel design to advance future lunar pit exploration efforts.

Design principle

The proposed wheel design used continuum deformation of the material to achieve shape transformation. This approach not only avoided the mechanical vulnerabilities of conventional joint components but also distributed strain uniformly, in contrast with compliant origami structures that concentrate strain in localized regions. This uniform strain distribution enabled large circular-to-circular volume transformations while mitigating the risk of failure under high mechanical loads or impacts.

The circular-to-circular volume transformation was facilitated by a coiling mechanism driven by the counterrotational motion of the left and right sides of the hub (Fig. 2Ai). The hub had a cylindrical structure with a separated middle section, where one side was freely rotatable and the other was fixed to the driving axis, allowing counterrotation between the two sides (Fig. 2Aii). Adjustments in the strip's rim and spoke ratio were achieved using a slit in the interweaving grouser block, enabling both interweaving with other strips and sliding motion (Fig. 2Aiii). This design ensured flexibility and adaptability, critical for robust performance in extreme lunar conditions.

When the wheel transitioned to the storage state, the diameter decreased, requiring the spoke portion of the strip to be decreased while the rim portion increased. Conversely, when transitioned to the deployment state, the spoke portion of the strip increased, and the rim portion decreased (Fig. 2B). The stress on the strip and its bending energy reached a minimum when deployment was complete and increased as the system moved toward the storage mode. The system passively returned to the lowest energy state, meaning that the wheel could be deployed without the need for an additional actuator (movie S1).

Figure 2C shows the detailed assembly sequence and storage mode. To assemble the strips and grousers with the hub, the ends of the strips were inserted into the hub. A wheel with a single strip could be coiled by the rotation of the hubs (Fig. 2Ci). Similarly, for a wheel with multiple strips (*N* strips) interwoven through the grouser's slit, coiling was achieved by hub rotation, just as with a single strip (Fig. 2Cii).

The key feature of the wheel was its resistance to shape changes under external loads while allowing easy volume modulation under torsional forces during folding. This was achieved through the characteristics of reciprocal structure. One of the main characteristics of the reciprocal structure applied to this design was that a single strip affected adjacent strips in a chain. Such structural behavior enabled a level of resistance to external loads that would be difficult to achieve with an individual strip alone.

This anisotropic property was critical for achieving efficient performance in deployable wheels. The performance analysis of the

deployable wheel focused on the torque required for storage and structural elasticity under vertical loads. Both the wheel's storage torque and structural elasticity were derived by the bending strain energy of the strips u, and u could be geometrically derived as follows:

$$u = \int_0^L \frac{B}{2}\left(\frac{\mathrm{d}\theta}{ds}(s) - \left(\frac{\mathrm{d}\theta}{ds}(s)\right)_0\right)^2 ds \quad (1)$$

where B is the flexural rigidity, that is, $B = EI/(1 - \nu^2)$ for wide beams (*41*). E is the Young's modulus of the material, I is the moment of inertia, and ν is the Poisson ratio of the material. The arc length measured from the end clamped to the grouser and the tangent angle of the centroidal axis of the strip are denoted by s and $\theta(s)$. Accordingly, $d\theta/ds$ represents the curvature of the strip, and $(d\theta/ds)_0$ denotes its value in the absence of external forces. The curvature directly determines the overall shape of the wheel.

First, to analyze the configuration and its properties of the deployment-storage process, a large deflection cantilever beam model was used (*42*, *43*), starting from the grouser's contact point with the strip and extending to the hub's fixed point with the strip (Fig. 3A). This geometric configuration model derived the curvature and bending moment from numerous combinations of design parameters, which included the hub radius (r_h) and the number, length, width, and thickness of the strips (N, L, b, and t). These results enabled capturing the bending behavior of the strip, providing an accurate representation of the strip's deflection, and helping to

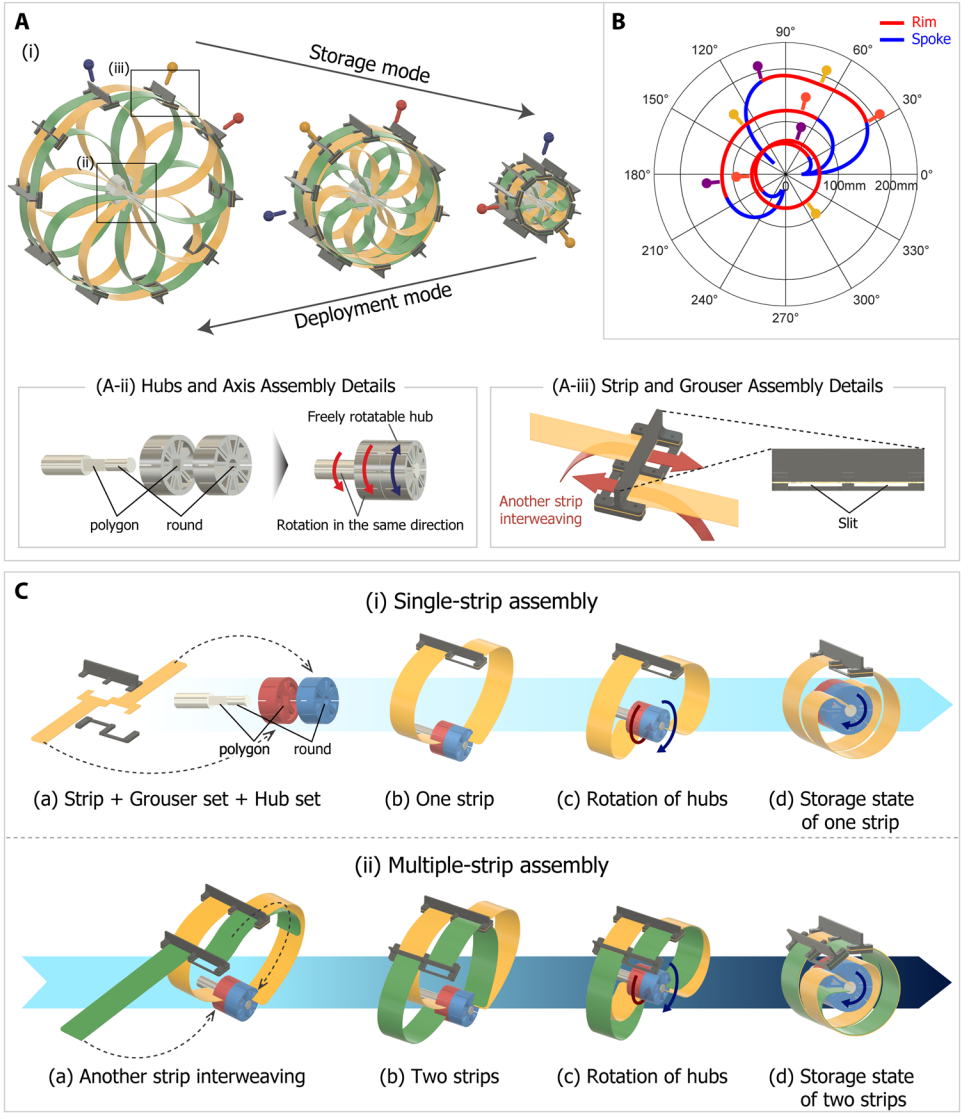

Fig. 2. Geometrical description of the wheel structure and coiling mechanism. (**A**) Soft deployable wheel structure with different shape modes: (i) coiling mechanism for deployment and storage, enabled by (ii) a specialized hub set, axis, and (iii) grouser design (the wheel model illustrated: hub radius, 30 mm; 10 strips; strip length, 200 mm; strip width, 30 mm). (**B**) Shape analysis of a single strip shown in (A). (**C**) Detailed description of wheel assembly sequence and coiling mechanism: (i) single-strip assembly and (ii) multiple-strip assembly.

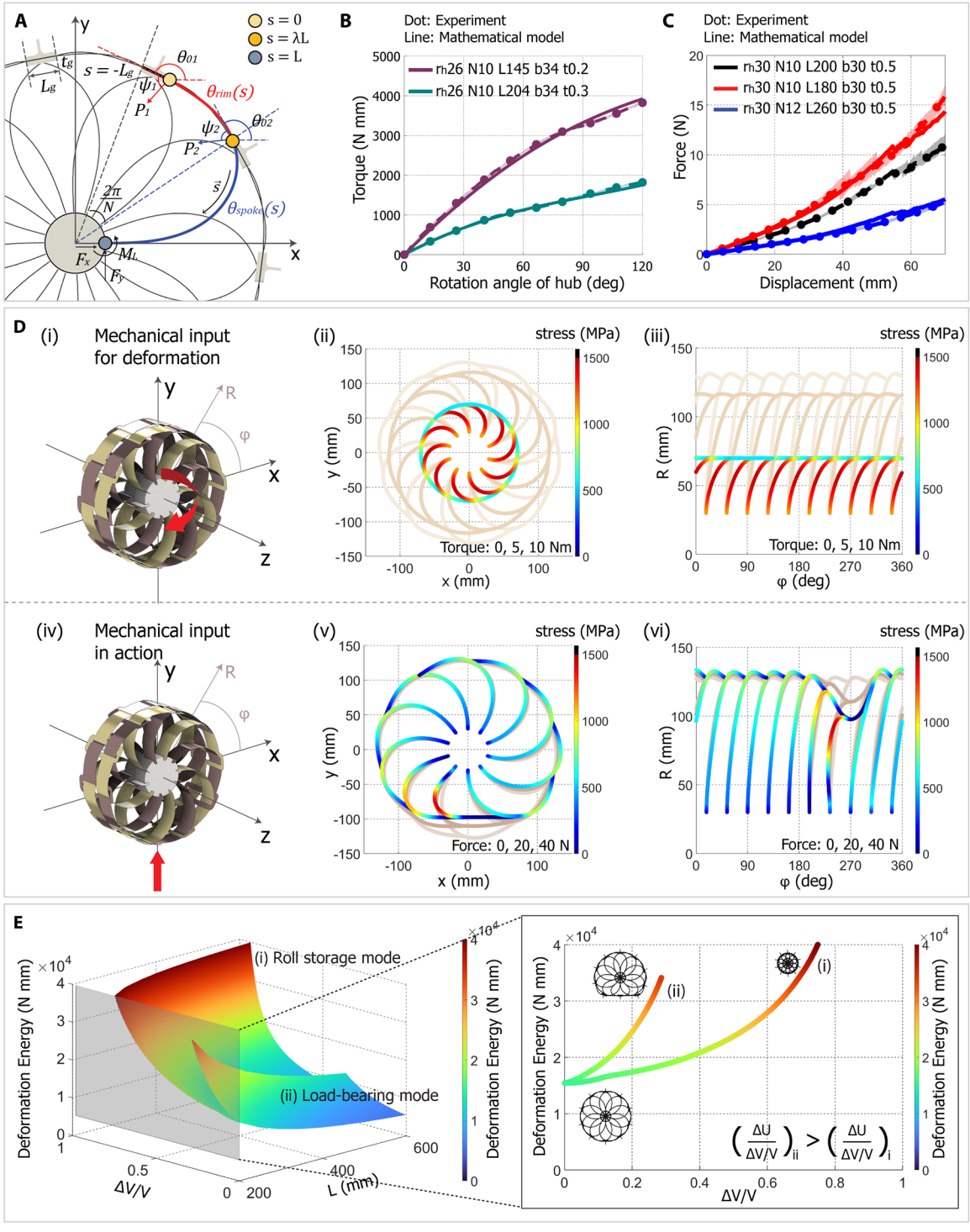

Fig. 3. Structural analysis of wheel. (**A**) Free body diagram (FBD) of cantilever beam for reciprocal soft deployable wheel structural analysis. (**B**) Validation of the FBD analysis through wheel transformation torque testing. (**C**) Validation of the normalized structural elasticity matrix ($\boldsymbol{E}_w$) through testing wheel load capacity. For both (B) and (C), the shaded bands indicate the full ranges (minimum to maximum) across repeated measurements, and the dotted lines denote the means ($n = 5$). (**D**) Shape and stress of the wheel in deployed, stowed, and vertically loaded states. (i) Deployed to stowed transition; (ii) Cartesian and (iii) polar representations from FBD analysis. (iv) Deployed to vertically loaded transition; (v) Cartesian and (vi) polar representations from multiflexible body dynamic simulation (model: [r_h30, *N*10, *L*200, *b*30, *t*0.4]). (**E**) Energy comparison in two different deformation modes, (i) storage and (ii) load-bearing capacity: The reciprocal structure enabled dual stiffness levels and anisotropic properties without the need for additional joints to adjust stiffness (model: [r_h30, *N*10, *L*200 to *L*600, *b*30, *t*0.4]).

analyze the wheel's performance. Accordingly, the wheel model was parameterized by the vector [r_h, N, L, b, and t]. For concision, specific designs were denoted as "model: [r_h30, N10, L200, b30, t0.4]," defined as a hub radius of 30 mm, 10 strips, a strip length of 200 mm, a strip width of 30 mm, and a strip thickness of 0.4 mm.

To apply the large deflection cantilever beam model, the variables and conditions were defined using a free-body diagram (Fig. 3A). The strip is interwoven with the adjacent front ($s = 0$) and rear ($s = \lambda L$) strips; accordingly, a single beam model contains three constraint points, including fixed point by hub at $s = L$. The model's primary variables are (P_1, ψ_1, P_2, ψ_2, and λ), and the grouser length and thickness (L_g and t_g) are treated as given parameters. The force applied at the first constraint point ($s = 0$) is denoted P_1 and acts at an angle ψ_1 measured counterclockwise from $\theta_{01}(=\theta(0))$. The force P_2 is applied to the second constraint point ($s = \lambda L$) at an angle ψ_2 measured counterclockwise from $\theta_{01}(=\theta(\lambda L))$. The variable λL represents the relative position of P_2 with respect to P_1 along the arc-length coordinate s. At the third constraint point ($s = L$), the force components F_x and F_y and the moment M_L depend on the primary variables. Through the model analysis, a unique solution for the function $d\theta/ds$ could be determined at a specific value of λ (Supplementary Methods; eqs. S1 to S16 describe more details of model analysis). These relations were evaluated using MATLAB (fig. S2) to compute the curvature and bending moment for the specified design parameters. To validate these results, torque testing served as an effective approach because the storage torque was directly determined by the evolving geometry during the deployment-storage process. Accordingly, wheel storage torque tests were conducted to validate the reliability of the calculation method (Fig. 3B). The excellent consistency with the torque test validated the accuracy of the deployment-storage configuration analysis, thereby supporting the reliability of the "Roll storage mode" analysis (Fig. 3Ei) used to characterize the anisotropic property shown in Fig. 3E.

The second analysis focused on the wheel's deformation under external vertical loading from the ground. In the proposed soft structure, the applied force (F_i) increased displacement (Δy_i) as in a spring model, but the relationship was not strictly linear. In such a complex nonlinear spring model, it was challenging to derive an explicit relationship between the design parameters and the load capacity. To facilitate the analysis of this nonlinearity, the individual elements of the original linear spring model were reformulated in vector form:

$$\boldsymbol{F_n} = \boldsymbol{k_n}\Delta\boldsymbol{y_n}, \begin{cases} \boldsymbol{F_n} = \left[F_1 \cdots F_i \cdots F_n\right]^T \\ \Delta\boldsymbol{y_n} = \left[\Delta y_1 \cdots \Delta y_i \cdots \Delta y_n\right]^T \\ \boldsymbol{k_n} = \mathrm{diag}\left[k_1 \cdots k_i \cdots k_n\right] \end{cases} \quad (2)$$

Each element in the vector was assumed to follow the linear spring model. The structural elasticity $\boldsymbol{k_n}$, defining the stiffness of the soft wheel in terms of the force-displacement relationship, was a key parameter for analyzing wheel performance and played an essential role in calculating strain energy under vertical loading. However, because of its numerous nonlinear elements and dependence on the wheel's multiple interrelated design parameters, $\boldsymbol{k_n}$ was difficult to compute directly from the wheel's geometry, making intuitive design highly impractical. To address this issue, a normalization method with respect to wheel scale was applied. The normalized structural elasticity matrix ($\boldsymbol{E}_w$) was defined to be dimensionless to ensure consistent properties across different wheel scales resulting from varying design parameters, and it can be obtained from load test for any wheel sample. R_d and u_0 represent the wheel radius and its strain bending energy in the deployment state, respectively. This approach allowed stiffness as a function of the design parameters to be estimated from load test data of a wheel sample, which could be presented in the following form:

$$\boldsymbol{F_n} = \boldsymbol{E}_w \frac{u_0}{\left(R_d - r_h\right)^2}\Delta\boldsymbol{y_n} \quad (3)$$

where $\boldsymbol{F_n}$ and $\Delta\boldsymbol{y_n}$ are vectors of applied force and displacement and $\boldsymbol{E}_w u_0/(R_d - r_h)^2$ is $\boldsymbol{k_n}$ (Supplementary Methods; eqs. S17 and S18 describe detailed derivation of Eq. 3). Wheel load tests were conducted to validate Eq. 3 (Fig. 3C). In addition to the torque test, the good agreement with the load test further supported the reliability of the "load-bearing mode" analysis (Fig. 3Eii) related to the anisotropic property presented in Fig. 3E. Figure 3D illustrates the strip positions and stress in both Cartesian (x-y) and polar (φ-R) coordinates in the deployed, stowed, and vertically loaded states of the wheel.

A comparison of the energy required for volume changes in storage mode and the vertical load state, using the validated methods, revealed that less energy was needed for storage, whereas more energy was required to support vertical loads (Fig. 3E). These results indicated that the structure features both easy storability and high load-bearing capacity. By applying the reciprocal structure, we achieved two different stiffness levels in two distinct deformation modes, resulting in an anisotropic structure, despite using a single material and no hinge components.

Parametric characterization

Deployment ratio (D_d/D_s) and $\boldsymbol{k_n}$ were set as key parameters for the wheel performance analysis. This section presents an analysis of the method for selecting design parameters that satisfy the prescribed performance requirements, D_d/D_s and $\boldsymbol{k_n}$. These performance requirements were influenced by both the flexural rigidity (B) of the flexible strips and the shape of the wheel structure. Among the wheel's design parameters, b and t were parameters of the flexural rigidity and could be easily calculated for the key parameters ($I = bt^3/12$). Given that $\boldsymbol{k_n}$ was proportional to EI, it follows that $\boldsymbol{k_n}$ was proportional to bt^3. With respect to the deployment ratio, the upper bound of allowable bending curvature ($d\theta/ds|_{max}$) was determined by the material's yield stress (σ_{yield}) and the strip thickness t. On the basis of this criterion, the minimum storage diameter D_s could be determined with t. The L_g and t_g parameters affected only the magnitude of the storage torque, with a negligible effect on both D_d/D_s and $\boldsymbol{k_n}$. The parameter b did not affect D_d/D_s.

The design parameters r_h, N, and L determined the shape of the wheel in the x-y cross section. Because N is a discrete variable, it could be analyzed by selecting values such as 8, 10, or 12; by contrast, the relationship between r_h, L, and the performance parameters was difficult to express explicitly and had to be obtained numerically. To present a method for selecting appropriate design parameters that satisfy the required wheel performance, there was a need to group design parameters sharing the same performance requirements and to systematically classify the implicit relationships. On the basis of the wheel configuration and structural elasticity calculation methods validated in the "Design principle" section, it was shown that with N and b fixed, any wheel model in which r_h, L, and

t are uniformly scaled by a factor $p > 0$ had the same D_d/D_s and $\boldsymbol{k_n}$. Specifically, comparing model 1 [r_h, N, L, b, t] with model p [pr_h, N, pL, b, pt], it was found that [r_h, L] corresponded to D_{d1}, whereas [pr_h, pL] corresponded to pD_{d1}. Given that D_s and $d\theta/ds|_{max}$ have an inverse relationship, the models [r_h, L, t] and [pr_h, pL, pt] shared the same D_d/D_s. According to the $\boldsymbol{E_w}$-based spring model (Eq. 3), the structural elasticity of model 1 ($\boldsymbol{k_{n,1}}$) and model p ($\boldsymbol{k_{n,p}}$) were also identical

$$\boldsymbol{k_{n,p}} = \boldsymbol{E}_w \frac{u_{0,p}}{\left(R_{d,p} - r_{h,p}\right)^2} = \boldsymbol{E}_w \frac{p^2 u_{0,1}}{p^2\left(R_{d,1} - r_{h,1}\right)^2} = \boldsymbol{k_{n,1}} \quad (4)$$

This comparison-based grouping approach was validated experimentally (Supplementary Methods and fig. S3). An increase in the performance parameter D_d/D_s enhanced the traversal ability for a given rover's storage volume. Similarly, a higher $\boldsymbol{k_n}$ increased the capacity to carry scientific equipment, enabling a broader range of mission capabilities. This implied that performance improved with increasing values of the flexible strip design parameters [N, L, b, t]. However, weight must be considered as a critical design constraint in the design process to select an appropriate scale. Here, the normalized weight parameter (W) is defined as the product $NLbtg_0$ with normalized density 1 g/cm^3(= 1000 kg/m^3) and gravitational acceleration g_0 (m/s^2). This definition was based on the weight of strips with normalized density and constant width, which are the main components of the deployable wheel structure.

By appropriately adjusting the design parameters related to weight, wheel models with identical performance parameters for a specific weight W were grouped for integrated analysis. As previously mentioned, models in which [r_h, L, t] were related by the same positive scalar multiple, with identical N and b, shared the same performance parameters. By combining the [r_h, L, t] to eliminate the positive scalar p, models were grouped using the dimensionless ratios [L/r_h, t/L, r_h/t]. These variables—L/r_h, t/L, and r_h/t—are not independent; determining two of them fixes the third variable. Consequently, among wheels designed with different geometric parameters, matching any two of these variables implies identical performance parameters. Figure 4 presented the performance parameters as functions of two selected dimensionless ratios. To incorporate the weight constraint W on the design, the relationship between W and the dimensionless ratios was expressed as

$$\frac{W}{r_h^2} = \frac{NLbtg_0}{r_h^2} = N\left(\frac{L}{r_h}\right)^2 \frac{t}{L} bg_0 \quad (5)$$

When $L/r_h = x$ and $t/L = y$, each line in the graph of $y = \text{Constant}/x^2$ represented a group with a constant W/r_h^2, N, b, g_0. These graphs showed the appropriate values for L and t that satisfy the weight constraint and the required performance parameters for a specified r_h during the design process (Fig. 4, A and B). We analyzed that there was a trade-off between the deployment ratio and structural elasticity when using only the design parameters r_h, L, and t. Increasing the width b proportionally enhanced only the structural elasticity, thereby expanding the performance limits (Fig. 4C). As the number of strips N increased, the performance improved under the same weight constraint W (Fig. 4, D to F). In Fig. 4, the structural elasticity, k, was treated as a constant by using the initial linear region of the response curve. However, the weight of the

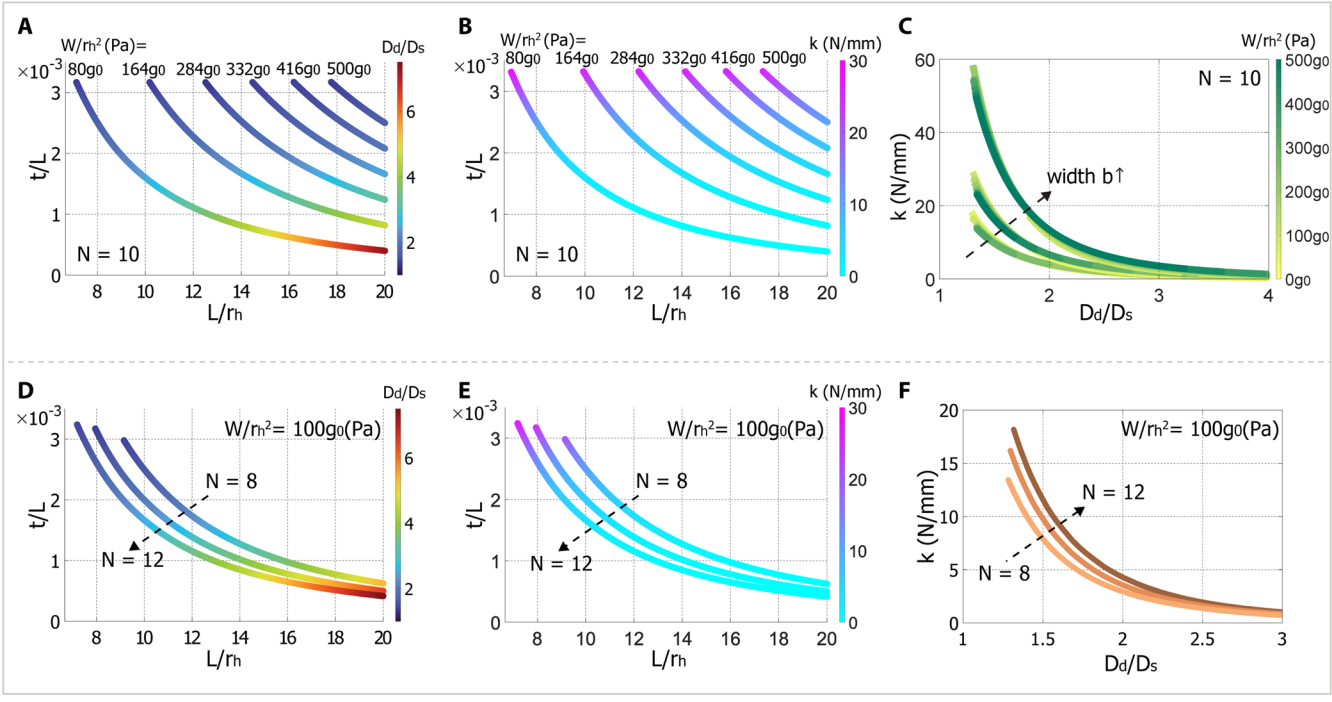

Fig. 4. Analysis results with design parameters L/r_h and t/L. (**A**) How to select design parameters to achieve required W and wheel performance D_d/D_s and (**B**) structural elasticity (b = 50 mm). (**C**) Trade-off in D_d/D_s and structural elasticity: Width b expanded performance limits (b = 30, 50, and 100 mm). Increasing strip number N improved performance (**D**) D_d/D_s and (**E**) structural elasticity (b = 50 mm). (**F**) As N increased, the performance limits expanded, but there was a risk of an increase in overall wheel weight that was not reflected on the graph (b = 50 mm).

grousers was not included in W, and as N increased, the number of grousers also increased, leading to a rise in the overall wheel weight. Therefore, careful adjustment was needed during the design process.

These analytical methods provided guidance for designing wheel structures to meet mission-specific requirements. The process began by defining three primary parameters: deployed diameter D_d, D_d/D_s, and target stiffness k_{target}. As an example case, we considered a 10-kg two-wheeled rover with $D_d = 450$ mm, $D_d/D_s = 2.5$, and a vertical displacement limit of 10% of D_d, resulting in a target stiffness of $k_{target} = 1.089$ N/mm. Two initial geometric parameters—the number of strips ($N = 10$) and the hub radius ($r_h = 30$ mm)—were selected by considering trade-offs among circularity, mass, and mobility stability. A lower number of strips reduced the effective circularity of the wheel, leading to increased geometric irregularity and dynamic instability. In contrast, a larger N increased the overall structural mass because of the increased number of grousers. Although a smaller r_h was beneficial in terms of wheel weight and performance, it must also ensure secure anchoring of the strips at the wheel center and maintain structural integrity by preventing shaft deformation between the hub and the motor.

By solving the beam model, the required strip length $L = 365$ mm was obtained for the specified D_d. From Fig. 4A, a material-limited maximum thickness of $t_{max} = 0.6$ mm was determined to satisfy $D_d/D_s = 2.5$. Applying a safety factor of 1.5 resulted in the selection of a safe working thickness of $t = 0.4$ mm. Using Fig. 4B, the corresponding strip width that satisfies k_{target} was calculated as $b = 57.4$ mm (see the "Design workflow" section in Supplementary Methods for more details). These parameters were derived on the basis of the material properties of heat-treated SK-5 steel, with Young's modulus $E = 194$ GPa and $\sigma_{yield} = 1567$ MPa.

The proposed wheel structure maintained a consistent geometric form across a variety of flexible sheet materials, enabling fabrication with alternative materials suited to specific environmental requirements. The allowable thickness of the strip is proportional to σ_{yield}/E; materials with a higher ratio permit greater thickness and maximum curvature, which enhances both structural load capacity and deployment ratio for a given constraint parameter W.

Several plastic-based materials considered for space applications offer relatively high σ_{yield}/E values compared with metals, enabling the use of thicker strips (see table S3). However, because of their generally lower Young's modulus, stiffness compensation must be achieved by increasing the strip thickness, given that stiffness is proportional to the moment of inertia ($\propto t^3$). In certain cases, PEEK (polyetheretherketone) offered a more favorable stiffness-to-weight characteristic, which is advantageous for lightweight wheel designs. Specifically, it resulted in a 28% weight reduction compared with a spring steel (SK-5) structure of equivalent stiffness while also achieving a 10% increase in allowable curvature. This increase in allowable curvature is particularly important, because it improves both the deployment ratio and the maximum load capacity. Kapton performs reliably across a wide temperature range, including high temperatures (*44*), whereas Teflon and Mylar (*45*) retain flexibility at cryogenic temperatures. These diverse material properties expand the applicability of the proposed structure across a range of extreme mission environments.

Thermal characterization

Thermal behavior is an important consideration in the design of space systems, affecting both structural reliability and mission operations. To analyze the thermal characteristics of the deployable wheel, a 42-day mission profile was established for the outer rim of the Marius Hills Pit. The thermal environment was modeled using "Thermal Desktop," incorporating the thermophysical and thermo-optical properties of the lunar regolith—including density (ρ), thermal conductivity (k_{re}), specific heat ($c_{v,re}$), and albedo (A)—which were defined as depth (z)—and temperature-dependent functions (Fig. 5A) (*46*–*48*). The regolith model had a radius of 5 m and a depth of 2 m, with parameters such as solar absorptance (α), albedo (*49*), surface emissivity (ε = 0.97) (*50*), and a subsurface heat flow of 0.018 W/m^2 applied (Fig. 5B) (*51*).

Temporal variations in total solar irradiance, elevation angle (θ_A), and azimuth angle (θ_Z) were incorporated into the model over the entire mission period (Fig. 5C) (*52*, *53*). The resulting thermal response of the wheel structure was assessed at sunrise, noon, and sunset, revealing substantial temperature gradients across the system (Fig. 5D). At noon, the wheel structure exposed to sunlight experiences substantially higher temperatures than that in shaded regions, resulting in considerable temperature gradients in the structure. The material composition and temperature sensor locations of each component are shown in Fig. 5E. On the basis of these sensor locations, the grouser labeled G2, shielded at noon, cooled to ~348 K—about 145 K lower than its exposed counterpart G1—and subsequently warmed to ~433 K because of lateral radiation, conductive heat transfer, and reflected solar input (Fig. 5Fi). Similarly, strips S2 and S3 remained around 343 K at noon because of solar shielding (Fig. 5Fii), whereas the hub, mostly obstructed by other components, exhibited a relatively low peak temperature of 425 K (Fig. 5Fiii) (see the "Details of thermal characterization" section in Supplementary Methods for more information on the thermal analysis).

Operating soft robots in the extreme thermal environment of space posed notable challenges. Thermal analysis suggested several critical operational strategies. The wheel's temperature exceeded 400 K throughout the lunar day, primarily because of the thermo-optical properties of its constituent materials. The deployable soft wheel proposed in this study could be fabricated from elastic plates made of various materials, enabling the use of options that remain resilient at elevated temperatures. One major concern was heat conduction from the wheel hub, which could cause motor overheating. To mitigate this risk, high-performance thermal-insulation pads, such as Bakelite or ceramic washers, could be inserted between the hub and the motor, limiting heat transfer and ensuring reliable actuation.

During the lunar night, the wheel was expected to cool to ~100 K. Operability at this temperature was achieved by selecting metals such as stainless steel (SUS) and other candidates that preserved mechanical integrity at cryogenic conditions, because the wheel architecture itself accommodated a wide range of flexible strip materials for additional optimization. Tape spring elements, in particular, had long served as hinge members in spacecraft mechanisms, including orbiting satellites and deployable antennas, and were documented to maintain reliable, large-amplitude bending performance even under deep cryogenic exposure, underscoring their suitability for the present wheel design (*54*). Although the structure could survive such low temperatures, cryogenic exposure had historically jeopardized the embedded electronics of conventional small rovers, prompting a variety of survival strategies in past missions. Instead of adding active heaters, the mission used a daytime-only, multirover strategy that completed all surface operations including cave entry within the thermally favorable window of lunar daylight.

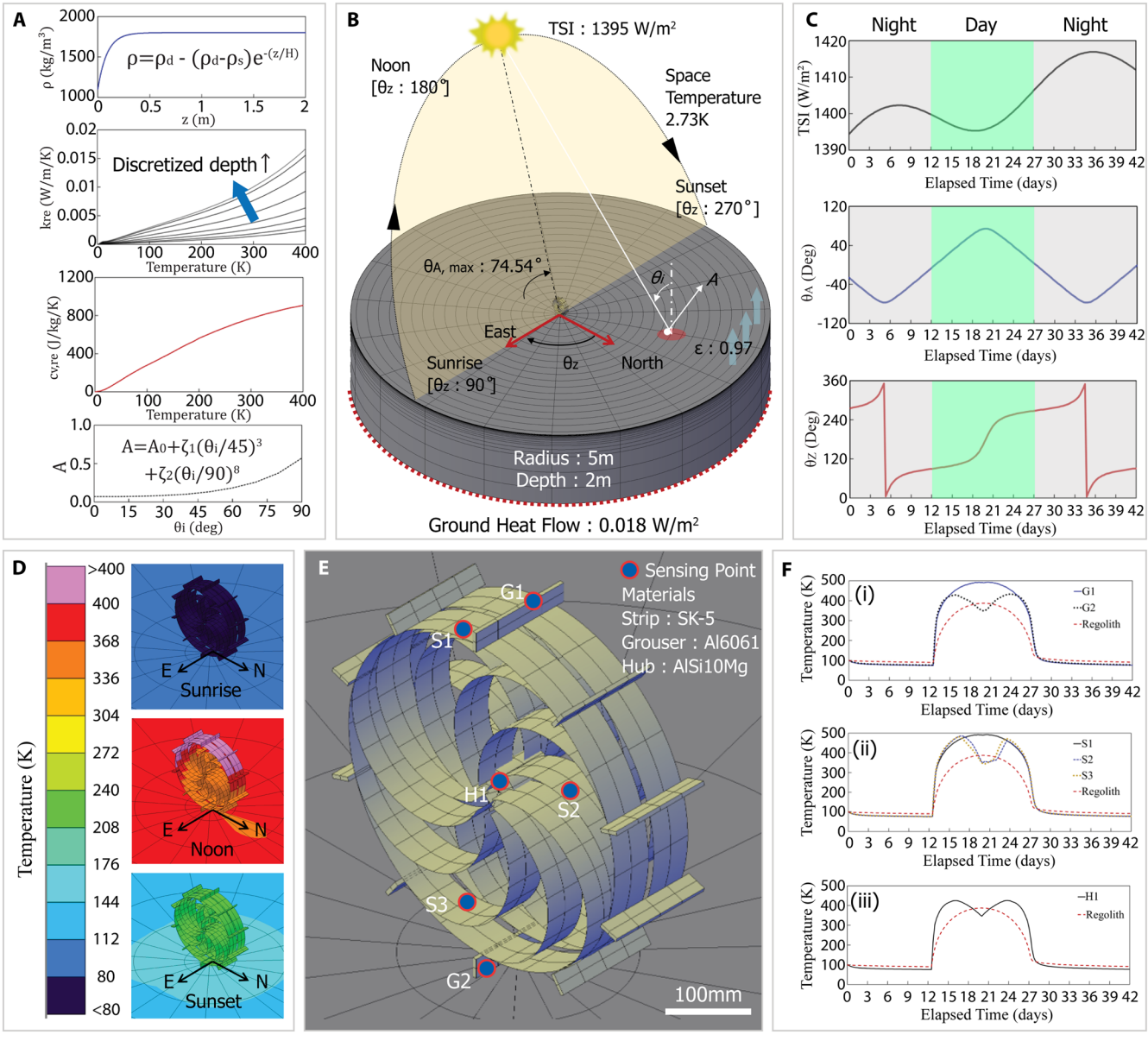

Fig. 5. Thermal analysis conditions and results of wheel. (**A**) Thermo-physical and thermo-optical properties of lunar regolith in the mission area. (**B**) Lunar regolith thermal model, analysis conditions, and solar radiation. (**C**) Total solar radiation, solar elevation, and solar azimuth angle over a 42-day mission period. (**D**) Thermal analysis results presented temperature contours of the wheel at different times of the lunar day: sunrise, noon, and sunset. (**E**) Wheel thermal model expanded from (B), showing material composition and temperature sensing points; sun-exposed and self-shaded locations were labeled as G1 and G2 on grousers and S1 to S3 on strips. Scale bar, 100 mm. (**F**) Temperature variations at each sensing point in (E); (i) grousers, (ii) strips, and (iii) hub.

The wheel's unique geometry created shaded regions that generated temperature gradients of up to 150 K across the structure. In general, these temperature gradients could lead to uneven thermal expansion and potential cold welding at contact interfaces. However, one of the key strengths of our wheel design was that it incorporated built-in tolerances at the hub connection and between adjacent metal strips, effectively accommodating thermal strain and preventing thermal binding. In addition to geometric tolerances accommodating thermal strain, continuous contact with regolith further hindered the formation of cold-welded junctions, enhancing the wheel's thermal robustness.

Experimental validation

Among the harsh environmental conditions encountered during lunar lava tube exploration, two representative and critical factors—thermal vacuum and drop impact—were selected for endurance testing. Five sample wheels were fabricated for testing. The grouser was made of aluminum 6061; the hub was produced using aluminum-based metal 3D printing; and the strip was manufactured from SK-5, a thin and flexible steel plate. The sample wheels have a model [r_h26, N10, L171, b34, t0.2], where D_d is 224.18 mm and D_s is 86.68 mm.

For the thermal vacuum test, each sample was exposed to a temperature of 423 K at 10^{-1} torr for 24 hours (test A) (Fig. 6A). After that,

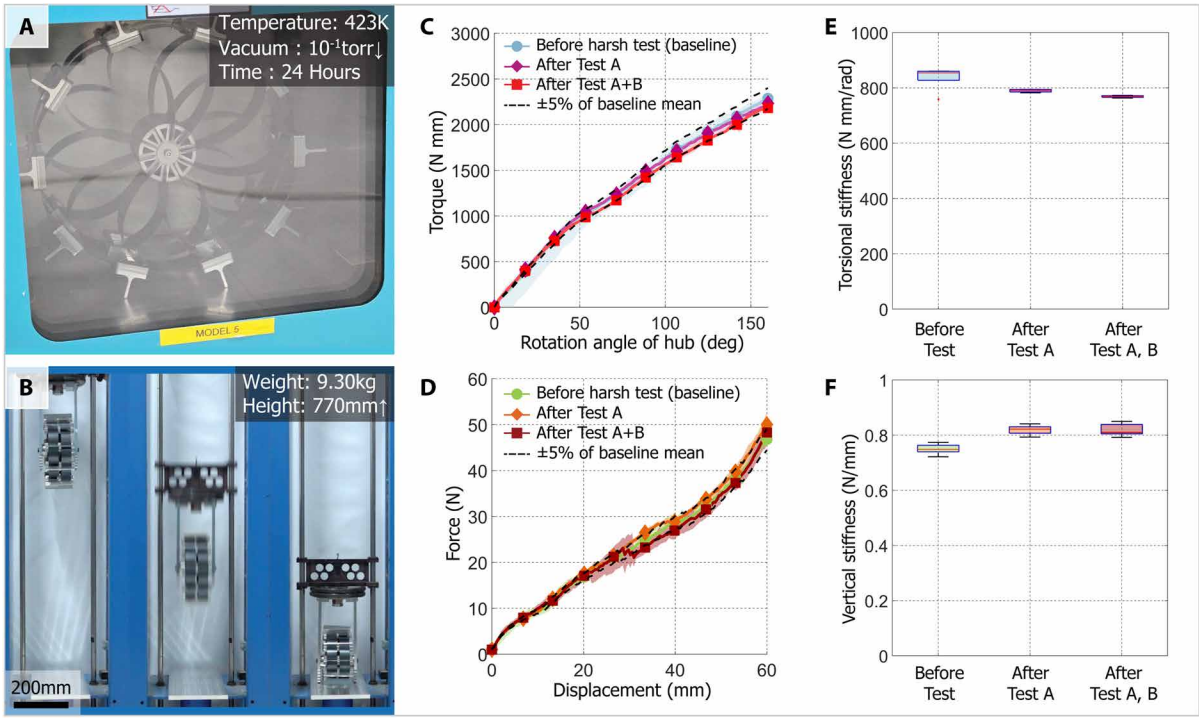

Fig. 6. Experimental validation of mission scenario feasibility. Two critical tests: (**A**) thermal vacuum chamber test at 423 K under 10^{-1} torr and (**B**) vertical drop impact test with 9.30 kg, above 770-mm height, were conducted. Scale bar, 200 mm. (**C**) Storage torque and (**D**) vertical load capacity of a single sample were compared. For both (C) and (D), the shaded bands indicate the full ranges (minimum to maximum) across repeated measurements, and the marked lines denote the means [$n = 1$ (sample) × 5 (repetitions) = 5], demonstrating consistent performance within ±5% (dotted line) of before the two harsh tests. (**E**) Torsional stiffness during storage and (**F**) vertical stiffness under payload for five samples were compared using box plots. For both (E) and (F), boxes represent the interquartile range (Q1 to Q3), the line inside each box indicates the median, and the whiskers denote the full range (minimum to maximum) of the experiment's data [$n = 5$ (samples) × 5 (repetitions) = 25], demonstrating the wheel's robustness under harsh conditions and supporting its potential for lunar lava tube exploration missions.

a total weight of 9.30 kg, including the wheel, was vertically dropped from a height of more than 770 mm (test B) (Fig. 6B). This impact is similar to the impact generated when a 4-kg two-wheeled rover lands after a 100-m vertical drop in the lunar gravity environment

$$\begin{cases} (mv)_{\text{moon}} = m\sqrt{2gh} = 4.00(\text{kg})/2 \cdot \sqrt{2 \cdot 1.63(\text{m/s}^2) \cdot 100(\text{m})} \\ \qquad = 36.1\ (\text{N} \cdot \text{s}) \\ (mv)_{\text{test}} = m\sqrt{2gh} = 9.30(\text{kg}) \cdot \sqrt{2 \cdot 9.81(\text{m/s}^2) \cdot 0.770(\text{m})} \\ \qquad = 36.1\ (\text{N} \cdot \text{s}) \end{cases} \quad (6)$$

During the vertical drop test, the allowable displacement was limited to $(R_d - R_s)$ with a support structure, which generalized the strip thickness and maximum bending curvature. Here, R_d is the wheel radius in the deployed state, and R_s is the wheel radius in the storage state. The wheel's main performance parameters, storage torque and load capacity, were compared across the samples. Figure 6 (C and D) shows the storage torque and load capacity for a single sample, which remained within ±5% of their initial values after tests A and B. Figure 6 (E and F) illustrates the torsional stiffness for storage and the vertical stiffness for payload weight of all five samples using box plots.

After the thermal vacuum and vertical drop-impact tests, a single-wheel drawbar pull test was conducted on simulated lunar regolith (Fig. 7, A and B). To ensure that the wheel interacted only with the soil and not with the underlying surface, the regolith was layered to a thickness greater than the wheel radius. During the test, both the drawbar pull force and the drive motor torque were acquired (Fig. 7, C and D).

On the basis of a 4-kg two-wheeled rover model, the slip ratio on a level surface was found to remain below 0.15, indicating stable traction in regolith terrain. Inclined driving was feasible when the drawbar pull force exceeded the downslope component of weight, $W\sin\phi$, where W denotes the weight and ϕ denotes the slope angle of terrain. From the experimental results shown in Fig. 7C, the wheel was determined to be capable of ascending slopes of up to approximately $\phi \approx 10°$ under Earth gravity when mounted on a 4-kg two-wheeled rover while maintaining a slip ratio of 0.5 or less. These results demonstrate that the proposed soft deployable wheel provided sufficient traction and slope climbing performance even in simulated lunar regolith, validating its terrain adaptability for potential deployment in lunar lava tube exploration.

Field test

The two-wheeled dummy rover system was prepared for the wheel's field performance evaluation. The system was primarily composed of an EPS (electrical power system), a communications module, and control and drive modules. In addition, it was equipped with light-emitting diode lights and a camera to facilitate navigation in caves. The power system (EPS) included a battery that served as the primary power source, providing energy to all subsystems. A converter regulated the voltage to ensure stable power delivery to the motor driver,

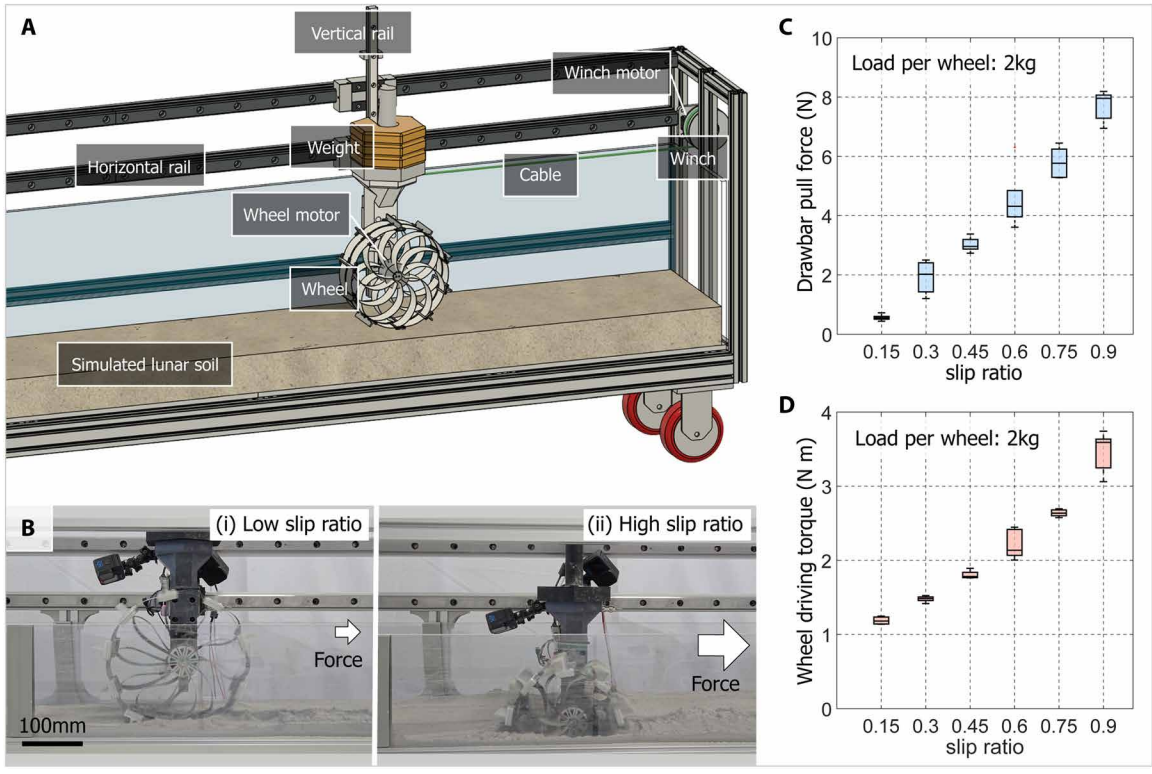

Fig. 7. Drawbar pull test and traversability evaluation in simulated lunar regolith. (**A**) A drawbar pull force testing platform was developed to evaluate performance in simulated lunar regolith terrain. Drawbar pull force was computed from winch torque and its radius. Vertical and horizontal rails accommodated sinkage and constrained forward driving motion. The simulated lunar regolith, KOHLS-1 (Korea Hanyang Lunar Simulant-1), was layered to a depth greater than the wheel radius to avoid floor contact. (**B**) Photographs from the drawbar pull force test at different slip ratios. Scale bar, 100 mm. (i) Low slip ratio showed minimal sinkage; (ii) high slip ratio showed substantial sinkage. (**C**) Drawbar pull versus slip ratio and (**D**) driving torque versus slip ratio were measured [$n = 1$ (samples) $\times$ 5 (repetitions) = 5, each slip ratio], indicating sufficient traction to climb 10° slopes as well. For both (C) and (D), boxes represent the interquartile ranges (Q1 to Q3), the line inside each box indicates the median, and the whiskers denote the full range (minimum to maximum) of the experiment's data.

sensors, and communication devices. The communication module handled remote control and data transmission, with an antenna that managed signal transmission and reception between the rover and the lander. The rover was equipped with a camera and lights to perceive the external environment and collect data. This configuration enables visual data collection in dark terrains such as caves.

The control and drive system managed the rover's mobility and posture control. The controller used a radiation-hardened 32-bit MCU (microcontroller unit), the RH32F, whereas the ADIS16505, commonly used in CubeSats, was used as the IMU (inertial measurement unit) to provide attitude data. On the basis of these data, the controller sent driving commands to the motor driver. The motor driver controlled two independent BLDC (brushless direct current) motors, each connected to a wheel, allowing precise movement and directional changes. The system, using flexible wheels, relied on IMU attitude data to achieve stable navigation on the lunar surface environment (Fig. 8A).

The rover equipped with deployable wheels demonstrated stable driving performance on simulated lunar soil terrain, which was challenging to traverse because of its dusty conditions and sand traps (Fig. 8B and movie S2). Such performance was typically unattainable with conventional joint-based structures, which rely heavily on tolerances and lubrication. We confirmed that the rover maintained its operational integrity after drop impacts from a height of 4 m under Earth's gravitational conditions (Fig. 8C and movie S3). Such impacts would likely have caused malfunctions in conventional joints, which were smaller and weaker. The large deployable diameter of the wheel not only avoided sand traps but also enabled effective traversal over rigid obstacles. This rover successfully climbed a 200-mm stair-like obstacle with a 34° incline, demonstrating its robust climbing capabilities (Fig. 8D).

The proposed wheel can be fabricated from a variety of flexible sheet materials, including steel. This flexibility in material selection allows customization to meet the demands of specific mission environments. For our tests, we used durable and resilient carbon steel, which enabled stable performance against the impacts and friction encountered in rigid, irregular terrains such as caves (Fig. 8E and movie S4). Furthermore, the fabricated carbon steel wheel demonstrated high-temperature resistance, ensuring its operability even in extreme fire environments (Fig. 8F and movie S5). The results highlighted the deployable wheel's ability to combine adaptability, durability, and operational efficiency, making it a promising solution for diverse and challenging mission scenarios.

DISCUSSION

In this study, we introduced a soft, deployable airless wheel specifically aimed at addressing the challenges of lunar lava tube exploration.

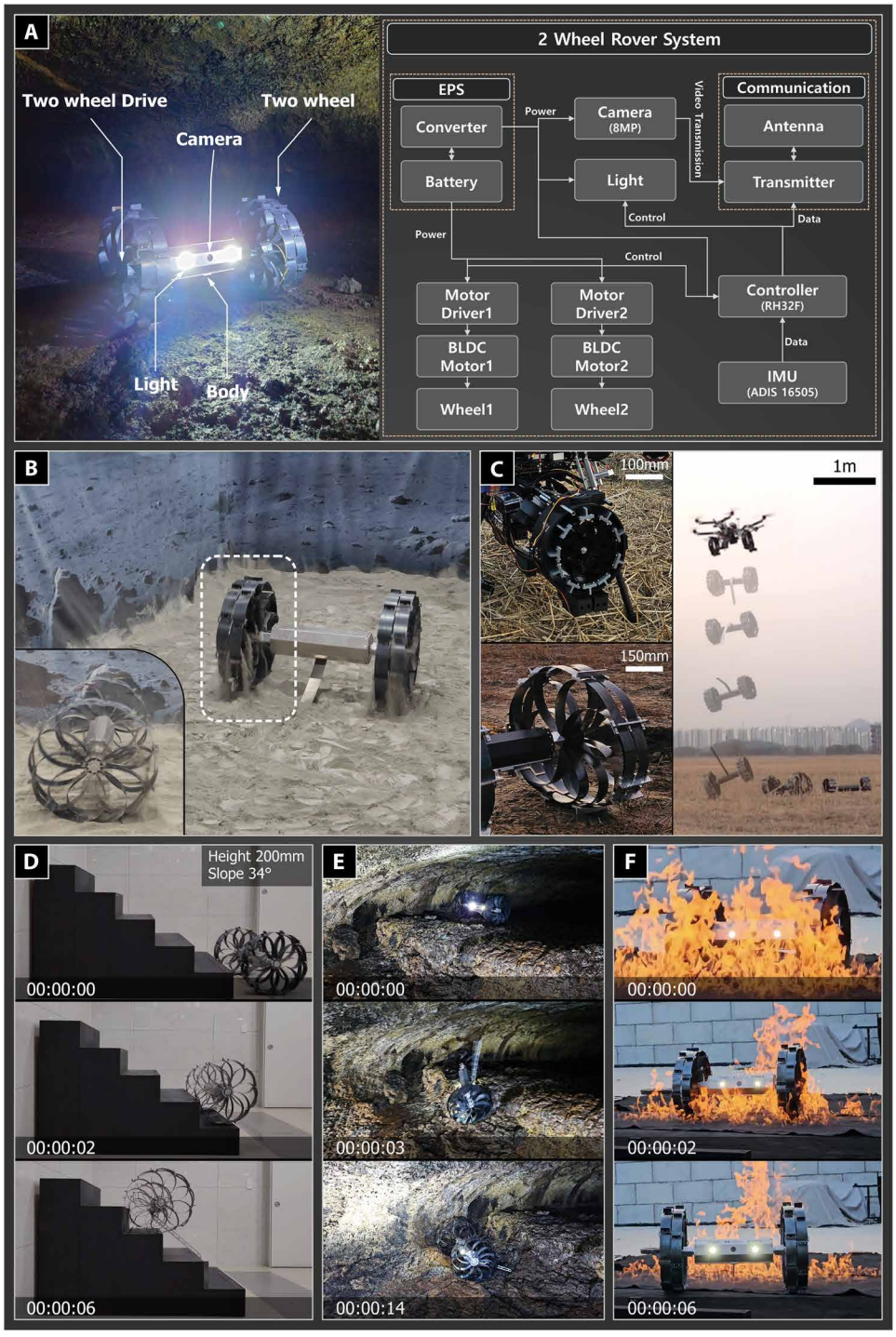

Fig. 8. Rover system configuration and field test. Field testing of the two-wheeled dummy rover equipped with soft deployable wheels was conducted for performance evaluation in extreme conditions. (**A**) The system configuration, including power, communication, control, and drive modules, was designed to support navigation and mobility in lunar cave environments. (**B**) Traversal on simulated lunar soil demonstrated stability in dusty conditions and resistance to sand traps. (**C**) An impact resilience test verified the rover's structural integrity after a 4-m drop under Earth's gravity (stowed state scale bar, 100 mm; deployed state scale bar, 150 mm; drop test scale bar, 1 m). (**D**) A climbing capability assessment showed that the rover successfully overcame a 200-mm stair-like obstacle with a 34° incline. (**E**) Performance validation on irregular rocky terrain inside a terrestrial cave simulated lunar cave conditions. (**F**) A high-temperature resistance test confirmed the wheel's durability in extreme thermal environments.

Lunar pit exploration is important for deciphering the Moon's geological history, understanding lava activity, and assessing the potential of lunar pits as natural shelters from space radiation and harsh thermal environments on the surface. Considering current crewed missions like Artemis, studying pit craters is both timely and valuable. Unlike terrestrial robotics, space robotics demands a substantially higher degree of reliability: A single failure can jeopardize the entire mission. Although lunar lava tubes have garnered substantial interest for their potential as future habitats, their direct exploration has been limited not only by factors such as precision landing and navigation but also by the absence of robust hardware systems capable of safely traversing steep funnels and vertical cliffs. We believe that our proposed wheel design provides a step toward mitigating this hardware gap.

We want to emphasize that a key aspect of our approach is its foundation in soft robotics. By harnessing structural deformations, we simplified overall system complexity and reduced the number of potential failure points. Whereas soft robotic systems were sometimes perceived as fragile because of the use of highly flexible materials, prior research demonstrated that having fewer components could increase robustness in extreme conditions. For space applications, where each actuator, sensor, or joint can introduce a new failure mode, the minimized complexity of soft robotics is particularly advantageous. However, adapting soft robotics to space presents substantial material challenges. Conventional elastomer-based soft robots often suffer from outgassing or radiation-induced degradation, making them unsuitable for vacuum environments. In addition, excessive flexibility can result in unpredictable motion, undermining reliability. To address these issues, our design used elastically deformable metal strips arranged in a helical, interwoven structure, enabling substantial shape change within minimal material strain. This configuration preserved structural integrity while striking an effective balance between deformation ratio and stability. Consequently, the wheel could absorb impacts and navigate uneven terrain while remaining robust under extreme lunar conditions.

Although our research has not yet produced a space-grade rover system, the wheel's modular nature allows it to be mounted on various microrovers without imposing substantial structural or mechanical burdens on the main rover. We anticipate integrating it into a space-ready microrover system and coordinating with a main rover to refine mission scenarios for actual lunar lava tube investigations. By demonstrating how soft robotic principles can be adapted to harsh environments through careful material selection and structural design, our work highlights the potential of soft robotics to expand the operational envelope of space missions.

MATERIALS AND METHODS

Fabrication

The deployable wheel presented in this study consists of three main components: the hub, grousers, and strips. For the wheels used in thermal vacuum and impact environment tests, the hub was manufactured using aluminum-based metal powder through metal 3D printing (AlSi10Mg, Staco Inc.). The grousers were fabricated from Al 6061 using computer numerical control (CNC) machining. For field tests and additional verification, the hubs and grousers were produced using a 3D printer (Onyx Pro, Markforged) with Onyx carbon fiber filament.

The strips used for the wheels in analytical validation of torque for storage mode (Fig. 3B), validation of design parameter grouping (fig. S3), thermal vacuum tests (Fig. 6), drawbar pull force test on simulated lunar soil (Fig. 7), all field tests (Fig. 8), and the analysis for maximum load capacity (fig. S5) were fabricated from heat-treated SK-5 carbon steel (Wang Special Steel Co.), with a Young's modulus of 194 GPa, a Poisson's ratio of 0.2786, and a yield strength of 1567 MPa. The strips for analytical validation of vertical load (Fig. 3C) and the validation for the analysis of maximum curvature (fig. S5C) were fabricated from 0.5-mm PET-G (polyethylene terephthalate glycol) film. All strips were processed using the VLS6.75 laser cutting system (Universal Laser System).

The wheels mounted on the rover were designed with a diameter of 500 mm to overcome obstacles as high as 200 mm and were fabricated using strips with a thickness of 0.4 mm and a width of 50 mm, resulting in an assembled wheel width of 100 mm. For experimental validation, smaller wheels were produced to fit the test setup. Specifically, the wheel specimens used in Fig. 3C to validate the theoretical stiffness equations were fabricated without rigid grousers, and holes were added to the strips to enable interweaving. These models were designed to isolate and analyze the properties of the strips alone for validation purposes.

Experimental setup

To evaluate the torque in storage mode and force in load-bearing mode, we used dedicated equipment tailored for each measurement. To measure the torque relative to the hub's rotation angle, we designed a rotational mechanism incorporating aluminum profile frames and gears machined from engineering plastics. This mechanism was designed to control the rotation of the free-rotatable hub using an XM540-W270-R motor (Robotis). Torque and angle measurements were recorded using a torque sensor (TRD605-160 N.m, Futek). Assembly details of each component are presented in fig. S7. Data acquisition was performed in real time at a rate of 400 Hz using LabVIEW software and a data acquisition system (National Instruments USB-6341).

For stiffness measurements in load-bearing mode, we used a tensile-compression testing machine (MCT-2150 W, A&D Company) equipped with a dedicated sensor offering a resolution of 0.01 N and a maximum capacity of 500 N. The analysis was conducted using the proprietary software (MSAT-Lite) provided by the manufacturer (A&D Company). A custom jig for securing the wheel was fabricated from aluminum 6061 using CNC machining, and tests were conducted at a low speed of 30 mm/min.

For the thermal-vacuum test, a vacuum chamber (DFZ-6020, Henan Lanphan Industry Co. Ltd.) was connected to an oil rotary high vacuum pump (W2V20, WSA Co. Ltd.). The dimensions of the chamber's interior were 300 mm by 280 mm by 300 mm ($W \times D \times H$), and wheel specimens were designed and fabricated to fit these constraints. The vacuum pump achieved a maximum vacuum level below 10^{-3} torr. Drop impact tests were conducted using a vertical rail apparatus capable of a maximum height of 1.6 m, ensuring that the wheel specimens were dropped vertically.

The internal dimensions of the drawbar pull force test bed (Fig. 7) are 3 m in length, 0.3 m in width, and 0.35 m in height. The system is designed to control the wheel's driving speed and slip ratio via a cable-driven mechanism. For the terrain environment, the simulated lunar soil KOHLS-1 (Korea Hanyang Lunar Simulant-1), developed in South Korea, was used. This simulant, first developed in 2009, has a composition ratio similar to NASA's Lunar Soil 14163, which was collected during the Apollo missions. The same simulant

was used in the traversal experiment shown in Fig. 8B. In Fig. 7, the soil depth was set to 150 mm, deeper than the wheel radius, to ensure full wheel-soil interaction. The test setup includes a travel motor (XM540-W270-T, Robotis) for wheel actuation at 10 rpm and a cable control motor (XM430-W350-T, Robotis) for slip and velocity adjustment. The cave exploration (Fig. 8E) was approved by the Jeju Special Self-Governing Province of the Republic of Korea.

Statistical analysis

All box plots follow standard conventions: The median is indicated by a line inside the box, the box height represents the interquartile range (Q1 to Q3), and the whiskers denote the minimum and maximum values. All continuously plotted experimental line graphs follow the same convention: The shaded region indicates the range between the minimum and maximum values, whereas the dotted line represents the average torque. To enhance the visibility of the mean trend, markers were added at regular intervals along the average curve. Unless noted otherwise, one sample per model was tested five times, and graphs show the mean with either the range (minimum to maximum) or interquartile range. The "Experimental conditions and data analysis procedures" section in Supplementary Methods provides comprehensive methodological details and data-processing protocols for each experiment in the main text and Supplementary Methods.

Supplementary Materials

The PDF file includes:
Methods
Figs. S1 to S7
Tables S1 to S4
References (*55*–*60*)

Other Supplementary Material for this manuscript includes the following:
Movies S1 to S5

REFERENCES AND NOTES

1. D. G. Angelis, J. W. Wilson, M. S. Clowdsley, J. E. Nealy, D. H. Humes, J. M. Clem, Lunar lava tube radiation safety analysis. *J. Radiat. Res.* **43**, S41–S45 (2002).
2. M. S. Robinson, J. W. Ashley, A. K. Boyd, R. V. Wagner, E. J. Speyerer, B. R. Hawke, H. Hiesinger, C. H. Van Der Bogert, Confirmation of sublunarean voids and thin layering in mare deposits. *Planet Space Sci.* **69**, 18–27 (2012).
3. I.-S. Hong, Y. Yi, E. Kim, Lunar pit craters presumed to be the entrances of lava caves by analogy to the Earth lava tube pits. *J. Astron. Space Sci.* **31**, 131–140 (2014).
4. E. R. Jawin, S. N. Valencia, R. N. Watkins, J. M. Crowell, C. R. Neal, G. Schmidt, Lunar science for landed missions workshop findings report. *Earth Space Sci.* **6**, 2–40 (2019).
5. R. V. Wagner, M. S. Robinson, Lunar pit morphology: Implications for exploration. *J. Geophys. Res. Planets* **127**, e2022JE007328 (2022).
6. J. J. Wynne, T. N. Titus, A. Agha-Mohammadi, A. Azua-Bustos, P. J. Boston, P. de León, C. Demirel-Floyd, J. De Waele, H. Jones, M. J. Malaska, Fundamental science and engineering questions in planetary cave exploration. *J. Geophys. Res. Planets* **127**, e2022JE007194 (2022).
7. T. Horvath, P. O. Hayne, D. A. Paige, Thermal and illumination environments of lunar pits and caves: Models and observations from the Diviner Lunar Radiometer experiment. *Geophys. Res. Lett.* **49**, e2022GL099710 (2022).
8. A. X. Wilcoski, P. O. Hayne, C. M. Elder, Thermal environments and volatile stability within lunar pits and caves. *J. Geophys. Res. Planets* **128**, e2023JE007758 (2023).
9. R. V. Wagner, M. S. Robinson, Distribution, formation mechanisms, and significance of lunar pits. *Icarus* **237**, 52–60 (2014).
10. A. P. Rossi, F. Maurelli, V. Unnithan, H. Dreger, K. Mathewos, N. Pradhan, D.-A. Corbeanu, R. Pozzobon, M. Massironi, S. Ferrari, *DAEDALUS-Descent And Exploration in Deep Autonomy of Lava Underground Structures: Open Space Innovation Platform (OSIP) Lunar Caves-System Study* (2021); 10.25972/OPUS-22791.
11. J. Zevering, D. Borrmann, A. Bredenbeck, A. Nüchter, "The concept of rod-driven locomotion for spherical lunar exploration robots," in *2022 IEEE/RSJ International Conference on Intelligent Robots and Systems (IROS)* (IEEE, 2022), pp. 5656–5663.
12. P. F. Miaja, F. Navarro-Medina, D. G. Aller, G. León, A. Camanzo, C. M. Suarez, F. G. Alonso, D. Nodar, F. Sauro, M. Bandecchi, L. Bessone, F. Aguado-Agelet, M. Arias, RoboCrane: A system for providing a power and a communication link between lunar surface and lunar caves for exploring robots. *Acta Astronaut* **192**, 30–46 (2022).
13. I. A. D. Nesnas, L. Kerber, G. Sellar, T. Balint, B. Denevi, A. J. Parness, R. P. Kornfeld, M. Smith, P. McGarey, T. Brown, E. Sunada, K. A. Gonter, B. Hockman, P. Hayne, T. Horvath, J. B. Hopkins, A. E. Johnson, R. V. Wagner, Y. Cheng, A. G. Curtis, K. Zacny, M. Paton, K. V. Sherrill, Moon Diver: Exploring a pit's exposed strata to understand lunar volcanism. *Acta Astronaut* **211**, 163–176 (2023).
14. A. Braun, K. A. Carroll, A. Ermakov, Enhanced gravimetry traverse for the Endurance lunar rover. *LPI Contrib.* **2985**, 3052 (2023).
15. R. U. Sonsalla, S. Planthaber, R. Dominguez, A. Dettmann, F. Cordes, B. Huelsen, C. Schulz, P. Schoeberl, S. Kasperski, H. Wiedemann, "Towards a semi-autonomous robotic exploration of a lunar skylight cavity," in *2022 IEEE Aerospace Conference (AERO)* (IEEE, 2022), pp. 1–20.
16. G. Picardi, M. Chellapurath, S. Iacoponi, S. Stefanni, C. Laschi, M. Calisti, Bioinspired underwater legged robot for seabed exploration with low environmental disturbance. *Sci. Robot.* **5**, eaaz1012 (2020).
17. G. Li, T.-W. Wong, B. Shih, C. Guo, L. Wang, J. Liu, T. Wang, X. Liu, J. Yan, B. Wu, F. Yu, Y. Chen, Y. Liang, Y. Xue, C. Wang, S. He, L. Wen, M. T. Tolley, A. M. Zhang, C. Laschi, T. Li, Bioinspired soft robots for deep-sea exploration. *Nat. Commun.* **14**, 7097 (2023).
18. T. S. Vaquero, G. Daddi, R. Thakker, M. Paton, A. Jasour, M. P. Strub, R. M. Swan, R. Royce, M. Gildner, P. Tosi, EELS: Autonomous snake-like robot with task and motion planning capabilities for ice world exploration. *Sci. Robot.* **9**, eadh8332 (2024).
19. P. Arm, G. Waibel, J. Preisig, T. Tuna, R. Zhou, V. Bickel, G. Ligeza, T. Miki, F. Kehl, H. Kolvenbach, M. Hutter, Scientific exploration of challenging planetary analog environments with a team of legged robots. *Sci. Robot.* **8**, eade9548 (2023).
20. M. Ishida, D. Drotman, B. Shih, M. Hermes, M. Luhar, M. T. Tolley, Morphing structure for changing hydrodynamic characteristics of a soft underwater walking robot. *IEEE Robot. Autom. Lett.* **4**, 4163–4169 (2019).
21. D. S. Shah, J. P. Powers, L. G. Tilton, S. Kriegman, J. Bongard, R. Kramer-Bottiglio, A soft robot that adapts to environments through shape change. *Nat. Mach. Intell.* **3**, 51–59 (2021).
22. E. Sihite, A. Kalantari, R. Nemovi, A. Ramezani, M. Gharib, Multi-Modal Mobility Morphobot (M4) with appendage repurposing for locomotion plasticity enhancement. *Nat. Commun.* **14**, 3323 (2023).
23. I. Park, H. Yoon, S. Kim, H. S. Kim, T. Seo, Review on transformable wheel: Mechanism classification and analysis according to mechanical complexity. *Int. J. Precis. Eng. Manuf.* **26**, 737–755 (2025).
24. D.-Y. Lee, J.-K. Kim, C.-Y. Sohn, J.-M. Heo, K.-J. Cho, High–load capacity origami transformable wheel. *Sci. Robot.* **6**, eabe0201 (2021).
25. Y.-S. Kim, G.-P. Jung, H. Kim, K.-J. Cho, C.-N. Chu, Wheel transformer: A wheel-leg hybrid robot with passive transformable wheels. *IEEE Trans. Robot.* **30**, 1487–1498 (2014).
26. V. Asnani, D. Delap, C. Creager, The development of wheels for the Lunar Roving Vehicle. *J. Terramech.* **46**, 89–103 (2009).
27. J. Zhu, Y. Shen, P. Hao, J. Liu, Y. Li, K. Wang, M. Zou, Modeling of flexible metal wheel for pressurized lunar rover and traction performance prediction. *J. Field Robot.* **40**, 2030–2041 (2023).
28. M. Zou, J. Zhu, K. Wang, Y. Lin, J. Jin, L. He, Y. Qi, Design and mechanical behavior evaluation of flexible metal wheel for crewed lunar rover. *Acta Astronaut* **176**, 69–76 (2020).
29. S. Sivo, A. Stio, F. Mocera, A. Somà, A study of a rover wheel for Martian explorations, based on a flexible multibody approach. *Proc. Inst. Mech. Eng.* **234**, 306–321 (2020).
30. G. Sharma, S. Tiwary, A. Kumar, H. N. S. Kumar, K. A. K. Murthy, Systematic design and development of a flexible wheel for low mass lunar rover. *J. Terramech.* **76**, 39–52 (2018).
31. D. Cardile, N. Viola, S. Chiesa, A. Rougier, Applied design methodology for lunar rover elastic wheel. *Acta Astronaut* **81**, 1–11 (2012).
32. J.-Y. Lee, S. Han, M. Kim, Y.-S. Seo, J. Park, D. Il Park, C. Park, H. Seo, J. Lee, H.-S. Kim, Variable-stiffness–morphing wheel inspired by the surface tension of a liquid droplet. *Sci. Robot.* **9**, eadl2067 (2024).
33. H. Yoon, K. Lee, J. Lee, J. Kwon, T. Seo, The stiffness adjustable wheel mechanism based on compliant spoke deformation. *Sci. Rep.* **14**, 773 (2024).
34. T. Aoki, Y. Murayama, S. Hirose, Development of a transformable three-wheeled lunar rover: Tri-Star IV. *J. Field Robot.* **31**, 206–223 (2014).
35. A. Husain, H. Jones, B. Kannan, U. Wong, T. Pimentel, S. Tang, S. Daftry, S. Huber, W. L. Whittaker, "Mapping planetary caves with an autonomous, heterogeneous robot team," in *2013 IEEE Aerospace Conference* (IEEE, 2013), pp. 1–13.
36. W. Fink, V. R. Baker, D. Schulze-Makuch, C. W. Hamilton, M. A. Tarbell, "Autonomous exploration of planetary lava tubes using a multi-rover framework," in *2015 IEEE Aerospace Conference* (IEEE, 2015), pp. 1–9.
37. B. J. Morrell, M. S. da Silva, M. Kaufmann, S. Moon, T. Kim, X. Lei, C. Patterson, J. Uribe, T. S. Vaquero, G. J. Correa, Robotic exploration of Martian caves: Evaluating operational concepts through analog experiments in lava tubes. *Acta Astronaut* **223**, 741–758 (2024).
38. V. S. Varadharajan, G. Beltrame, A multi-robot exploration planner for space applications. *IEEE Robot. Autom. Lett.* **10**, 2446–2453 (2025).

39. W. L. Whittaker, H. L. Jones, J. S. Ford, R. V. Wagner, D. Domingue, Pit-MAGIC: Lunar pit morphology and geomechanics investigation via circumnavigation. *LPI Contrib.* **2697**, 1071 (2023).
40. J. Haruyama, K. Hioki, M. Shirao, T. Morota, H. Hiesinger, C. H. van der Bogert, H. Miyamoto, A. Iwasaki, Y. Yokota, M. Ohtake, T. Matsunaga, S. Hara, S. Nakanotani, C. M. Pieters, Possible lunar lava tube skylight observed by SELENE cameras. *Geophys. Res. Lett.* **36**, L21206 (2009).
41. K. E. Bisshopp, D. C. Drucker, Large deflection of cantilever beams. *Q. Appl. Math.* **3**, 272–275 (1945).
42. B. S. Shvartsman, Large deflections of a cantilever beam subjected to a follower force. *J. Sound Vib.* **304**, 969–973 (2007).
43. M. Mutyalarao, D. Bharathi, B. N. Rao, Large deflections of a cantilever beam under an inclined end load. *Appl. Math. Comput.* **217**, 3607–3613 (2010).
44. DuPont, "Kapton HN Data Sheet" (2024); https://www.qnityelectronics.com/content/dam/electronics/amer/us/en/electronics/public/documents/en/EI-10206-Kapton-HN-Data-Sheet.pdf.
45. D. L. Lowe, D. L. Edwards, "Thermal testing of aluminized Mylar," NASA-TM-108414 (NASA, 1993).
46. P. O. Hayne, J. L. Bandfield, M. A. Siegler, A. R. Vasavada, R. R. Ghent, J. Williams, B. T. Greenhagen, O. Aharonson, C. M. Elder, P. G. Lucey, D. A. Paige, Global regolith thermophysical properties of the Moon from the Diviner Lunar Radiometer Experiment. *J. Geophys. Res. Planets* **122**, 2371–2400 (2017).
47. A. Martinez, M. A. Siegler, A global thermal conductivity model for lunar regolith at low temperatures. *J. Geophys. Res. Planets* **126**, e2021JE006829 (2021).
48. R. Woods-Robinson, M. A. Siegler, D. A. Paige, A model for the thermophysical properties of lunar regolith at low temperatures. *J. Geophys. Res. Planets* **124**, 1989–2011 (2019).
49. A. R. Vasavada, J. L. Bandfield, B. T. Greenhagen, P. O. Hayne, M. A. Siegler, J. Williams, D. A. Paige, Lunar equatorial surface temperatures and regolith properties from the Diviner Lunar Radiometer Experiment. *J. Geophys. Res. Planets* **117**, E00H18 (2012).
50. B. C. Roberts, "Cross-Program Design Specification for Natural Environments (DSNE) Revision G," SLS-SPEC-159 (NASA, 2019).
51. M. G. Langseth, S. J. Keihm, K. Peters, Revised lunar heat-flow values. *Proc. Lunar Sci. Conf.* **3**, 3143–3171 (1976).
52. M. Kaczmarzyk, M. Gawronski, G. Piatkowski, "Global database of direct solar radiation at the Moon's surface for lunar engineering purposes," in *E3S Web of Conferences* (EDP Sciences, 2018), vol. 49, p. 00053.
53. L. Wald, "Basics in Solar Radiation at Earth Surface-Revised Version# 2," hal-02175988 (2019).
54. M. Thaker, S. J. Joshi, H. Arora, D. B. Shah, Tape spring for deployable space structures: A review. *Adv. Space Res.* **73**, 5188–5219 (2024).
55. D. Deng, H. Murakawa, Numerical simulation of temperature field and residual stress in multi-pass welds in stainless steel pipe and comparison with experimental measurements. *Comput. Mater. Sci.* **37**, 269–277 (2006).
56. DuPont, "Teflon PTFE," (DuPont, 2025); http://rjchase.com/ptfe_handbook.pdf.
57. M. Kucher, M. Dannemann, D. Peyrow Hedayati, R. Böhm, N. Modler, Experimental investigation of the vibration-induced heating of polyetheretherketone for high-frequency applications. *Solids* **4**, 116–132 (2023).
58. Gund Company, "Material Data Sheet" (Gund Company, 2025); https://datasheet.datasheetarchive.com/originals/crawler/thegundcompany.com/046a2a19b43841e9c77ae44a2ae1f92c.pdf.
59. DuPont Teijin Films, "Product Information Mylar " (2025); https://docs.rs-online.com/aafb/0900766b81111eb5.pdf.
60. M. A. Spivack, Mechanical properties of very thin polymer films. *Rev. Sci. Instrum.* **43**, 985–990 (1972).

Acknowledgments

Funding: This research was supported by the National Research Foundation of Korea (NRF) (no. 2022R1C1C1003718 and no. RS-2025-02213804), the Korea AeroSpace Administration (KASA) (no. RS-2024-00509485), the Korea Technology and Information Promotion Agency for SMEs (TIPA) (no. RS-2024-00511688), the Research of Future Challenge Innovation of the KARI (no. FR25T00), and the Brain Pool Plus Program through the National Research Foundation of Korea funded by the Ministry of Science and ICT (no. 2020H1D3A2A03099291). **Author contributions:** S.-B.L. created, designed, and developed the deployable wheel mechanism, conducted the theoretical analysis of wheel properties and characteristics, performed the experiments and data analysis, and wrote and edited the manuscript; N.C. developed the two-wheeled platform hardware system, built the field-test setup and environment, performed the experiments, validated the analysis data, provided resources, acquired funding, and wrote the manuscript; G.L. fabricated the wheels; S.L. and J.K. performed the experiments; G.S. developed the simulation, analyzed the data to evaluate the wheel's thermal characteristics, and wrote the manuscript; J.T.J. and S.K.K. acquired funding and reviewed and edited the manuscript; T.W.S. reviewed and edited the manuscript; C.K.S. conceptualized the mission, acquired funding, and wrote the manuscript; and D.-Y.L. created, designed, and developed the deployable wheel mechanism, supervised and administered the project, acquired funding, and wrote and edited the manuscript. **Competing interests:** S.-B.L., N.C., G.L., and D.-Y.L. are inventors on a patent (KR. 10-2688596) submitted by Korea Advanced Institute of Science and Technology and Unmanned Exploration Laboratory Co. Ltd. that covers the design of the deployable airless wheel structure. **Data and materials availability:** All experimental data and modeling code generated in this study have been deposited in Dryad at DOI: 10.5061/dryad.tdz08kqb4.

Submitted 6 March 2025
Accepted 18 November 2025
Published 17 December 2025
10.1126/scirobotics.adx2549

Science Robotics

Soft deployable airless wheel for lunar lava tube intact exploration

Seong-Bin Lee, Namsuk Cho, Geonho Lee, Seungju Lee, Junseo Kim, Gyujin Shim, Jong Tai Jang, Se Kwon Kim, TaeWon Seo, Chae Kyung Sim, and Dae-Young Lee

Sci. Robot. **10** (109), eadx2549. DOI: 10.1126/scirobotics.adx2549

Science Robotics (ISSN 2470-9476) is published by the American Association for the Advancement of Science. 1200 New York Avenue NW, Washington, DC 20005. The title *Science Robotics* is a registered trademark of AAAS.